Flow and fouling in elastic membrane filters with hierarchical branching pore morphology

Zhengyi Chen (陈征依),[1, a)] Shi Yue Liu (刘诗玥),[1, a)] Ivan C. Christov,[2] and Pejman Sanaei[3, b)]
[1)] *Fu Foundation School of Engineering and Applied Science, Columbia University, New York, NY 10027, USA*
[2)] *School of Mechanical Engineering, Purdue University, West Lafayette, Indiana 47907, USA*
[3)] *Department of Mathematics, New York Institute of Technology, New York, NY 10023-7692, USA*

(Dated: 3 June 2021)

Filtration is widely used in industry, therefore prediction of filtration efficacy and analysis of filter performance are essential. Real membranes have complex internal geometry: pores inside the membrane branch and interconnect with each other, which must be taken into account in mathematical models of filtration. Membrane fouling, as an unavoidable consequence of removing particles, occurs in the course of filtration and deteriorates the membrane permeability. In addition, for membranes made of elastic materials, the pressure within the membrane results in expansion of the pore radii. The pore expansion competes with particle deposition to delay fouling and, thus, influences filtration performance. In this paper, we develop a mathematical model of flow and fouling of such elastic membrane filters with multi-layer bifurcating (hierarchical) interior morphology. Two filtration forcing mechanisms through the membrane are considered: (i) constant pressure drop; and (ii) constant flux. We investigate how filtration behaves under these two forcing mechanisms and mathematically describe the morphology change due to fouling coupled to elastic pore expansion. In particular, we obtain an analytical solution for the deformation of the elastic pore walls, which is easily incorporated into the filtration model. Our model provides a quantitative mathematical framework with which to predict the impact of hierarchical pore morphology and the elasticity of pore walls on filtration performance.

I. INTRODUCTION

Filtration refers to a separation process that uses membrane filters to sieve undesired particles or contaminants from a fluid. The applications of filtration in industry are numerous[1], inspiring a substantial amount of fundamental research as well[2–8]. For instance, filtration is used to purify wastewater[9,10], in which particles including microbial contaminants are removed from the filtrate through micro-filtration or ultra-filtration. In the medical setting, filtration technology plays an important role in artificial kidneys and blood oxygenators[1]. Other applications include, but are not limited, to hot gas cleaning[11], protein purification and apple juice clarification[12].

Two prominent methods of filtration are: (i) cross-flow (tangential) filtration; and (ii) dead-end filtration[13]. In the first case, the direction of the flow is tangential to the membrane surface, while the flow is perpendicular to the surface and the fluid directly penetrates through the membrane in dead-end filtration. Furthermore, the membrane operation can also be classified by the flow's driving force. Specifically, membrane filtration is conventionally split into constant pressure and constant flow regimes. Note that, in all of these classifications, the overall requirement for filtration is to remove undesired particles (contaminants) from the carrier fluid, while maintaining low energy usage and cost. In this paper, we focus on dead-end filtration for the reason that this mechanism is more ubiquitous in practice and has the characteristic of high selectivity, economic scalability and lower energy cost compared with cross-flow filtration[14].

Ideally, it is desirable that all the solvent passes through the membrane filter, while all the undesired particles are retained in the membrane. However, as the filtration process proceeds, the particles can deposit on the pore walls within the membrane or block the pores' entries. This phenomenon is called membrane fouling and results in additional flow resistance across the whole system. Three mechanisms of fouling may occur separately or simultaneously during filtration: (i) particle adsorption (also called standard blocking), in which small particles adhere to the pore walls; (ii) blocking, in which large particles sit at the pores' inlets and block the pores partially or completely; and (iii) cake formation, which usually happens at the late stages of filtration, when the large particles block the pore entrance and form an additional cake layer on top of the membrane, which effectively acts as another membrane layer. An extensive review of modeling of pore-blocking behaviors of membranes during pressurized membrane filtration has been conducted by Iritani[3] and Grenier *et al.*[15]. They examined the three fouling mechanisms using experimental flux data to illustrate the relevance of each. Ho and Zydney[16] analyzed the transition between two fouling mechanisms and their combined impact on filtration performance. Sanaei and Cummings[17] considered standard blocking as the only fouling mechanism to demonstrate

[a)] These authors contributed equally to this work.
[b)] Electronic mail: psanaei@nyit.edu; https://sites.google.com/nyit.edu/pejman-sanaei-webpage

the pore morphology change due to small particle adsorption, which is the most prominent fouling mechanism and the only mechanism that makes full use of the pore interior. Intuitively, fouling will start at the pore inlet, lead to a shrinkage in the pore radius and finally will result in the closure of a pore. Therefore, this fouling mechanism controls the total filtration time and the amount of filtrate processed. According to Grace [18], fouling is dominated by the standard blocking mechanism until the late stages of the filtration process, hence we believe that it is reasonable to make a simplification and leave the effect of blocking and cake formation to future work. The effect of sieving by big particles is to increase the total system resistance, therefore the total throughput decreases. We may also observe that cake formation actually prolongs the lifetime of a filter, in the sense that the time to total blocking is longer relative to the case with no caking. However, there is a trade-off for this extended lifetime in terms of inefficiency: the flux through the filter drops rapidly and filtration is slow, even for situation in which the cake layer thickness is much less than the membrane thickness[6].

Some prior work used first-principles models to explain the dynamics involved in the filtration process. However, most of the literature employs an assumption of simple geometries, such as tubes spanning through the whole membrane. For example, Bruining [22] studied the fluid dynamics in a hollow fiber membrane. In industrial applications, the membrane's internal structure can be quite complicated, as shown in Fig. 1, featuring many branches and bifurcations. Such structures complicate the modeling of both feed solution flow and particle migration, but must be accounted for to make mathematical models realistic. In general, it is common that the pores' cross-sectional area is larger at the upstream compared to the downstream side, yielding an effective porosity gradient (defined as the local pore volume fraction in any small membrane element) through the depth of membrane[17]. It has been observed that this porosity gradient through the depth of the membrane yields better filtration performance for both removing contaminants, while also increasing the membrane lifespan. This enhancement phenomenon is due to the fact that fouling begins at the upstream side of the membrane, therefore the upstream pores shrink faster compared to the downstream ones[2,6,17,23–26].

Given this impetus to understand filtration processes with complex internal morphology, recent work has begun to provide insights. For example, Dalwadi, Griffiths, and Bruna [27] proposed a model of a membrane consisting of spherical obstacles of various sizes, with filtrate flowing across them externally. Another practical model is a multilayer structure that boosts the filtration performance. For example, Ling *et al.* [28] noted that, in water purification treatment, multilayer filters can promote filtration performance by increasing throughput, efficiency and loading capacity. Recent works[7,17,23] capture the depth variation of the pore structure, which is built into real membranes, allowing the pore sizes and connectivity to be a function of depth through the membrane. These works adopted a layered structure model, with changes in pore size/connectivity occurring at layer boundaries.

In this paper, we adopt the branching model proposed by Sanaei and Cummings [17], considering a series of bifurcating pores spanning the membrane, with decreasing radius through the depth of the membrane. Our model captures key features of filtration and its performance (specifically, the total amount of filtrate fluid and contaminant concentration in the filtrate). Under constant flux and pressure drop imposed on the filtration process, we consider the adsorption of small particles on the pore walls as the only fouling mechanism. More importantly, our model includes another factor that affects the pore radius evolution (as well as filtration performance): the elasticity of the membrane's pore walls. Note that most filtration models in the literature assume that the membrane pore walls are rigid. However, in reality many membrane filters are made of elastic materials, and pores expand due to flow forces[29,30]. For example, Herterich, Griffiths, and Vella [31] considered the poroelasticity of the pore walls, providing evidence for the hypothesis that elasticity prevents backflushing from cleaning clogged filters. Going further within this context of poroelasticity, Köry *et al.* [32] investigated how choosing an initial spatially-dependent permeability can lead to a uniformly permeable filter. They found a permeability distribution that maximizes the flux for a given applied pressure. They extended their framework to model cake filtration in a dead-end filter[33]. However, these poroelasticity models do not consider the deformation of individual pores (as in the example filter in Fig. 2), but rather how the whole porous structure respond to the total pressure drop.

This latter effect has been analyzed in related studies of flow-induced deformation of single cylindrical pores. Anand and Christov [34] obtained an analytical solution to the two-way-coupled fluid–structure interaction problem in a thin and slender tube, including shear-dependent viscosity effects and also hyperelastic[35] and viscoelastic[36] material response. Raj M *et al.* [37] proposed a simple analytical model that considers the effect of pressure-driven non-Newtonian flow in a cylindrical pore under one-way coupling. Karan *et al.* [38] reconsidered the problem with axial variations in the Young's modulus. Meanwhile Boyko, Bercovici, and Gat [39] discussed an unsteady version of the problem. The elasticity of branching pore structures has also been modeled[40,41] and experimentally interrogated[42] and found to have a significant impact on backflow through hydraulically fractures subsurface reservoirs (a porous medium much like membrane filters). Motivated by these results, in this paper, we investigate the competing effect between the flow-wise hydrodynamics-induced pore radius expansion (due to elasticity) and the shrinkage of the pore radius due to particle adsorption. In particular, we obtain an analytical solution to the deformation of the elastic pore wall, which is easily incorporated into the filtration model of

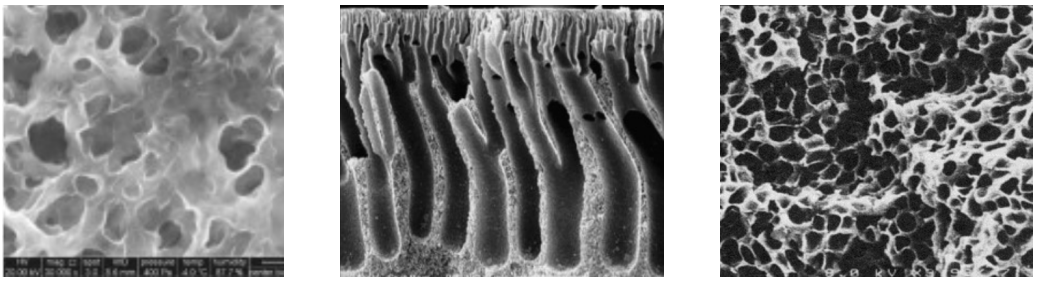

(a) (b) (c)

FIG. 1. Magnified membranes with various pore distributions, shapes, and sizes. (a), (b) and (c) are reproduced from Refs. 19, 20 and 21, respectively, with permission.

a hierarchical branching membrane.

The goal of this paper is to develop and analyze a branching model of an elastic membrane filter in which the flow and filtration process switches from a constant flux driving regime to a constant pressure regime. To this end, we analyze (i) the deformation of the elastic branching model caused by the flow pressure; and (ii) the filtration performance in both operation regimes. The paper is organized as follows: in §II, we introduce the mathematical model for flow in a bifurcating branching structure, as well as the governing equations of an elastic pore. In §III, we introduce appropriate scalings, for the two flow regimes of interest, to nondimensionalize the models from §II. Then, in §IV, we present simulations that address filtration performance, specifically the particle retention and the amount of filtrate fluid are calculated and analyzed. Finally, we summarize our modeling results in §V and provide some insight into real-world applications as well.

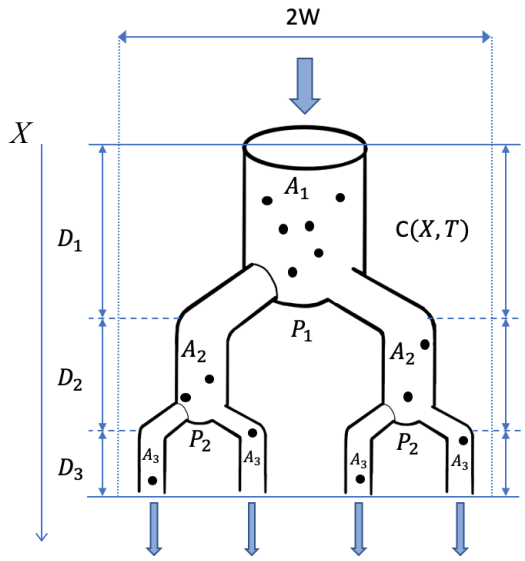

FIG. 2. Schematic of one unit (width $2W$) of a repeating branching structure with three layers ($m = 3$) of the type modeled herein. The thicknesses (resp. radii) of the three layers are denoted as D_1 (resp. A_1), D_2 (resp. A_2) and D_3 (resp. A_3), respectively. The pressures at the bottom of the first and second layers are P_1 and P_2. Particles at concentration $C(X,T)$ deposit onto the pores walls. The coordinate X denotes the total depth through the structure in the flow-wise direction.

II. MATHEMATICAL MODEL

As discussed in §I, the two common filtration scenarios considered herein are: (i) flow driven by a constant flux; and (ii) flow driven by a constant pressure drop across the membrane. In case (i), the pressure at the membrane inlet needs to increase or decrease to sustain the imposed flux as the membrane fouling or pore expansion, respectively, occurs during the filtration process. In case (ii), the flux will be reduced as the membrane is fouled. These two filtration scenarios are modeled through sets of assumptions that will be given in §§II A and II B, respectively. Further, in elastic membranes, the pores expands due to the hydrodynamic pressure within the membrane. The model for the pore radius expansion due to elasticity is described in §II C. Throughout, we use uppercase and lowercase letters to represent dimensional and dimensionless quantities, respectively.

Absorptive fouling, also known as standard blocking, is the dominant filtration mechanism, since it strongly depends on the membrane interior pore structure[43], which is also a feature of our branching model. Thus, we focus on fouling due to particle absorption within the membrane structure. We assume the membrane is flat (two-dimensional) and remains in the (Y, Z) plane. A unidirectional incompressible Darcy flow, with superficial velocity U, passes through the membrane in the positive X direction. The membrane morphology and properties are homogeneous in the (Y, Z) plane but vary in the X direction. The filtrate is assumed to contain particles, whose diameter is much smaller than the radius of all the interior pores in the membrane. Thus, the particles can pass through the (unfouled) filter easily. The particle concentration is given by C. As particles either pass

through the entire membrane or are captured by the internal pore walls, $C = C(X,T)$ will vary with the depth through the membrane X and time T. All particles are assumed to behave identically.

As shown in Fig. 1, the pore network morphology of membranes used in applications is quite complex. Pores with depth-dependent structure are interconnected and branch into further pores. Many membranes have large pores at the upstream end, which bifurcate into smaller pores towards the downstream end. We simplify the model by assuming that the membrane contains repeated units in a square lattice pattern, with period $2W$. The basic lattice unit is shown in Fig. 2. Each unit contains one cylindrical pore of length D_1 at the upstream side, which bifurcates into two smaller pores, moving down in the positive X direction. Each of the bifurcated pores further branches into smaller pores after a distance D_2, and the branching process continues until the downstream membrane end is reached. Therefore, each consecutive layer in the membrane contains twice the number of pores as the previous layer. The membrane is proposed to have m internal layers and the schematic in Fig. 2 is an example of a three-layer membrane.

Hence, for the general case, layer i contains $n_i = 2^{i-1}$ pores with depth D_i, and it occupies the domain $X_{i-1} \le X \le X_i$, with $X_i = \sum_{j=0}^{i} D_j$ (defining $D_0 = 0$ for convenience). We also use D to refer to the thickness of the membrane, with $D = \sum_{j=0}^{m} D_j$. Meanwhile, since the membrane is assumed to be elastic, the pores tend to expand due to the hydrodynamic pressure of the flow through the membrane. To ensure that the pores will not recombine at the downstream end, and that the sum of the radii of the pores should not exceed the period $2W$, the parameters of the model need to be carefully chosen and the methodology for doing so will be discussed in §IV.

A. Constant Flux Case

For filtration driven by a constant flux, we introduce the superficial (or, Darcy) velocity U through the membrane and the constant flux Q_{pore} through the branching structure. These are related as

$$(2W)^2 U = Q_{\text{pore}}, \quad \frac{\partial U}{\partial X} = 0, \tag{1}$$

where the second relation enforces the continuity equation. We define throughput as

$$V(T) = \int_0^T (2W)^2 U \, dT', \tag{2}$$

which is the total volume of filtrate processed up to time T. The quantity V is used in experimental studies to compare the performance of different filters. Equivalently,

$$\frac{dV}{dT} = (2W)^2 U, \qquad V(0) = 0. \tag{3}$$

Similarly, the cross-sectionally averaged pore velocity in the ith layer, $\bar{U}_{p,i}(X,T)$, is related to U via a flux balance argument (conservation of mass):

$$(2W)^2 U = \pi n_i A_i^2(X,T) \bar{U}_{p,i}(X,T), \quad 1 \le i \le m, \tag{4}$$

where $A_i(X,T)$ represents the pore radius in layer i. From equations (2), (4) and the Hagen–Poiseuille law[29], we further obtain

$$(2W)^2 U = -\frac{\pi}{8\mu} n_i A_i^4(X,T) \frac{\partial P(X,T)}{\partial X}, \quad 1 \le i \le m, \tag{5}$$

where $P(X,T)$ is the pressure within the branching structure, and μ is the fluid's dynamic viscosity. Note that the pressure gradient $\partial P/\partial X$ throughout the structure is not constant. Integrating both sides of (5) from X_{i-1} to X_i (i.e., across the depth of the membrane ith layer), we obtain

$$\begin{gathered} (2W)^2 U = -\frac{n_i}{\mu \mathcal{R}_i} \big[P_i(T) - P_{i-1}(T) \big], \\ X_{i-1} \le X \le X_i, \quad 1 \le i \le m, \end{gathered} \tag{6}$$

where P_i $(1 \le i \le m-1)$ are the unknown interlayer pressures within the membrane. In other words, $P_i(T) = P(X_i, T)$. Here, $P_0(T)$ is the pressure at the upstream side and $P_m = 0$ is the pressure at the outlet of the membrane. In (6), we have also introduced the hydrodynamic resistance of a single pore:

$$\mathcal{R}_i(T) = \int_{X_{i-1}}^{X_i} \frac{8}{\pi A_i^4(X,T)} dX, \quad 1 \le i \le m, \tag{7}$$

keeping in mind that we defined $D_0 = 0$ and $X_0 = 0$ above.

Applying (6) at each layer, along with (1), results in a system of m equations for U and P_i $(1 \le i \le m-1)$. If we solve the system successively for P_i, we obtain:

$$(2W)^2 U = \frac{P_0(T)}{\mu \mathcal{R}(T)}, \tag{8}$$

where

$$\mathcal{R}(T) = \sum_{i=1}^{m} \frac{\mathcal{R}_i(T)}{n_i} \tag{9}$$

captures the net resistance of the branching structure in terms of the resistances of its sublayers. Note that, we define the initial resistance of the total branching structure as $\mathcal{R}(0) = \mathcal{R}_0$.

The model presented in this subsection captures the Darcy flow through a membrane with a hierarchical branching structure. To explore how the membrane morphology evolves due to fouling during the filtration process, we must specify how particles deposit on the pore walls, and how the pore radii evolve due to particle deposition. Hence, the cross-sectionally averaged particle concentration in the pores of the ith layer, $C_i(X,T)$, needs

to be determined. In general, the small particles are advected and diffuse within the flow and adhere to the wall at a rate proportional to their local concentration. To represent these processes, within each pore, we use the prior models[2,26], which were derived by a careful asymptotic analysis of the advection–diffusion equation governing particle transport along the pores. These analyses revealed that (in a certain distinguished Péclet number limit) diffusion dominates in the radial direction, leading to the particle concentration being approximately uniform across the pore cross-section. Meanwhile, variation in concentration along the length of the pore is governed by an advection equation. We refer the reader to these papers for further details. This model was also used in a branching structure[17], and we employ it herein.

Specifically, the small particle concentration $C_i(X,T)$ in the ith layer is governed by an advection-reaction equation:

$$\bar{U}_{p,i}\frac{\partial C_i}{\partial X} = -\Lambda\frac{C_i}{A_i}, \quad X_{i-1} \le X \le X_i, \quad 1 \le i \le m, \tag{10}$$

where $\bar{U}_{p,i}$ is found from (4). The (dimensional) constant Λ captures the physics of the attraction between particles and the pore wall, which results in particle deposition. Equation (10) is subject to a boundary condition that specifies the particle concentration at the membrane inlet:

$$C_1(0,T) = C_0. \tag{11}$$

The continuity of particle concentration at the junction of each layer must also be enforced. Equation (10) can be solved analytically to yield:

$$C_i(X,T) = C_0 \exp\left(-\int_0^X \frac{\Lambda\, dX'}{A_i(X',T)\bar{U}_{p_i}(X',T)}\right), \tag{12}$$

for $1 \le i \le m$.

The pore radius $A_i(X,T)$ in the ith layer shrinks due to the deposition of small particles, as:

$$\frac{\partial A_i}{\partial T} = -\Lambda\alpha C_i, \quad X_{i-1} \le X \le X_i, \quad 1 \le i \le m, \tag{13}$$

for some constant α (proportional to the particle size). Equation (13) is based on the simple assumption that the pore cross-sectional volume per unit depth shrinks at a rate determined by the local volume of particles deposited. The initial condition for (13) is

$$A_i(X,0) = A_{i_0}, \quad X_{i-1} \le X \le X_i, \quad 1 \le i \le m, \tag{14}$$

where A_{i_0} is the (constant, specified) initial radius of the pores in the ith layer. At this point in the model, the elasticity of pores, which results in expansion of the pore radii, has not been taken into the account. This issue will be addressed in §II C.

B. Constant Pressure Case

All equations in §II A, i.e., (1)–(14), also hold for fixed-pressure-drop filtration, but the Darcy velocity $U = U(T)$ is a function of time now, the inlet pressure $P_0 = P_{\text{switch}}$ is constant, and therefore the flux Q_{pore} through the branching structure is no longer constant. When discussing our simulations in §IV below, we explain why we term the inlet pressure in this scenario as the 'switch' pressure.

C. Membrane Elasticity

In this subsection, the effect of elasticity on the pore radius within the branching structure is modeled. If the membrane material is elastic (as it is in many practical situations), then the pore walls will deform under the fluid pressure forces within the pores, especially as the pressure increases due to fouling. As shown in Fig. 2, each pore is basically a cylindrical exclusion. Since we assume that the membrane contains repeated units in a square lattice pattern, with period $2W$, it is reasonable to consider a symmetry (no stress) condition between adjacent lattices, otherwise the entire structure might undergo motion (displacement) in some direction, breaking the periodicity. Therefore, the pores' shrinkage or expansion in each layer does not affect the other pores in the same layer, given that they (and the flows through them) are all identical. Therefore, it is reasonable to assume that the deformation of one pore does not affect those nearby. Under this assumption, the deformation of each pore can be described by the Navier–Cauchy equations[44] (also known as Lamé's equations[45]). In the absence of body forces (gravitational forces are negligible at the pore-scale), these equations take the form

$$\frac{E}{2(1+\nu)}\nabla^2\boldsymbol{\Omega}_i + \frac{E}{2(1+\nu)(1-2\nu)}\boldsymbol{\nabla}(\boldsymbol{\nabla}\cdot\boldsymbol{\Omega}_i) = \rho_m\frac{\partial^2\boldsymbol{\Omega}_i}{\partial T^2}, \quad 1 \le i \le m. \tag{15}$$

Here, $\boldsymbol{\Omega}_i = (\Omega_{i_R}, \Omega_{i_\theta}, \Omega_{i_X})$ is the displacement vector of the pore in the ith layer in the cylindrical coordinates (R,θ,X). Futher, ρ_m denotes the density of the elastic material from which the membrane is composed, E is the Young's modulus, quantifying the compliance of the elastic solid material, and ν its Poisson's ratio, which quantifies the elastic solid's compressibility. Assuming that the time scale related to the pore wall deformation due to elasticity is longer than the time scale of the flow (which is the small Strouhal number limit discussed by Anand and Christov[36]), we can impose an elastostatic condition, i.e., $\partial^2\boldsymbol{\Omega}_i/\partial T^2 = 0$.

Under these assumptions, (15) simplifies to

$$\nabla^2\boldsymbol{\Omega}_i + \frac{1}{1-2\nu}\boldsymbol{\nabla}(\boldsymbol{\nabla}\cdot\boldsymbol{\Omega}_i) = \mathbf{0}, \quad 1 \le i \le m. \tag{16}$$

Based on the geometric setup of our model, we write the governing equation (16) in axisymmetric cylindrical coordinates, component-wise[45],

$$\nabla^2\Omega_{i_R} - \frac{\Omega_{i_R}}{R^2} + \frac{1}{1-2\nu}\frac{\partial}{\partial R}(\boldsymbol{\nabla}\cdot\boldsymbol{\Omega}_i) = 0, \tag{17}$$

$$\nabla^2\Omega_{i_X} + \frac{1}{1-2\nu}\frac{\partial}{\partial X}(\boldsymbol{\nabla}\cdot\boldsymbol{\Omega}_i) = 0, \tag{18}$$

for $1 \le i \le m$.

To define the boundary conditions for (17)–(18), we consider the normal stress $\boldsymbol{\Sigma}_i = (\Sigma_{i_R}, \Sigma_{i_\theta}, \Sigma_{i_X})$ at the ith layer pore wall. Under the assumption of a long and slender pore (to be made precise in §III C), it can be shown that that the shear stresses are negligible, and the radial normal stress Σ_{i_R} matches the hydrodynamic pressure imposed[34]. At the same time, a symmetry condition can be imposed on the stress between two adjacent lattice elements to ensure equal and opposite forces there. Furthermore, the pore in the ith layer is clamped on the top and the bottom of each layer. Therefore, the boundary conditions are:

$$\begin{aligned} \Sigma_{i_R}|_{R=A_i} &= P, \quad \left.\frac{\partial\Sigma_{i_R}}{\partial R}\right|_{R=W} = 0\,, \\ \Omega_{i_X}|_{X=D_{i-1}} &= 0, \quad \Omega_{i_X}|_{X=D_i} = 0, \quad 1 \le i \le m. \end{aligned} \tag{19}$$

Equations (17) and (18) can be solved with the boundary conditions (19) after re-expressing the normal stress $\boldsymbol{\Sigma}_i$ in terms of the displacement $\boldsymbol{\Omega}_i$. From the constitutive and strain–displacement relations of linear elasticity[44,45], the relationship between $\boldsymbol{\Sigma}_i$ and $\boldsymbol{\Omega}_i$ is:

$$\begin{aligned} \Sigma_{i_R} &= \frac{E(1-\nu)}{(1+\nu)(1-2\nu)}\frac{\partial\Omega_{i_R}}{\partial R} \\ &+ \frac{E\nu}{(1+\nu)(1-2\nu)}\frac{1}{R}\Omega_{i_R} + \frac{E\nu}{(1+\nu)(1-2\nu)}\frac{\partial\Omega_{i_X}}{\partial X}, \end{aligned} \tag{20}$$

$$\begin{aligned} \Sigma_{i_\theta} &= \frac{E\nu}{(1+\nu)(1-2\nu)}\frac{\partial\Omega_{i_R}}{\partial R} \\ &+ \frac{E(1-\nu)}{(1+\nu)(1-2\nu)}\frac{1}{R}\Omega_{i_R} + \frac{E\nu}{(1+\nu)(1-2\nu)}\frac{\partial\Omega_{i_X}}{\partial X}, \end{aligned} \tag{21}$$

$$\begin{aligned} \Sigma_{i_X} &= \frac{E\nu}{(1+\nu)(1-2\nu)}\frac{\partial\Omega_{i_R}}{\partial R} \\ &+ \frac{E\nu}{(1+\nu)(1-2\nu)}\frac{1}{R}\Omega_{i_R} + \frac{E(1-\nu)}{(1+\nu)(1-2\nu)}\frac{\partial\Omega_{i_X}}{\partial X}, \end{aligned} \tag{22}$$

for $1 \le i \le m$. Note that we have taken $\Omega_{i_\theta} = 0$ and $\partial(\cdot)/\partial\theta = 0$ for an axisymmetric pore geometry but, nevertheless, a "hoop stress" Σ_{i_θ} can arise from the axial and radial deformations.

III. SCALING AND NONDIMENSIONALIZATION OF THE MODEL

To reduce the number of independent parameters, we nondimensionalize the model for the (i) constant flux and (ii) constant pressure drop filtration scenarios described in §§II A and II B, respectively, using appropriate scalings introduced for each one below. For the elasticity equations from §II C, the only difference in the nondimensionalization of variables in the two cases is how we scale the normal stress $\boldsymbol{\Sigma}_i$ and the pressure P_i of a pore in the ith layer.

A. Flow: Constant Flux Case

We use the following scalings to nondimensionalize the model given by equations (1)–(14):

$$\begin{aligned} P_i &= \mu\mathcal{R}_0 Q_{\text{pore}} p_i, \\ (X, X_i, D_i) &= D(x, x_i, d_i), \\ C_i &= C_0 c_i, \\ (\mathcal{R}_i, \mathcal{R}) &= \mathcal{R}_0(\varrho_i, \varrho), \\ U &= \frac{Q_{\text{pore}}}{4W^2}u, \\ \bar{U}_{\text{p,i}} &= Q_{\text{pore}}\left(\frac{8\pi D}{\mathcal{R}_0}\right)^{-1/2}\bar{u}_{\text{p,i}}, \\ T &= \left(\frac{8D}{\pi\mathcal{R}_0}\right)^{1/4}\frac{1}{\Lambda\alpha C_0}t, \\ V &= \left(\frac{8D}{\pi\mathcal{R}_0}\right)^{1/4}\frac{Q_{\text{pore}}}{\Lambda\alpha C_0}v, \\ A_i &= \left(\frac{8D}{\pi\mathcal{R}_0}\right)^{1/4}a_i. \end{aligned} \tag{23}$$

With these scalings, we obtain the governing equations for $v(t)$, $\bar{u}_{p_i}(x,t)$, $\varrho(t)$, $p(0,t)$, $c_i(x,t)$ and $a_i(x,t)$ (i.e., throughput, averaged pore velocity, branching structure resistance, pressure at the pore inlet, averaged particle concentration and pore radius in ith layer, respectively) as

$$\frac{dv}{dt} = 1 = n_i a_i^2(x,t)\bar{u}_{p,i}(x,t), \tag{24}$$

$$\varrho_i(t) = \int_{x_{i-1}}^{x_i}\frac{dx}{a_i^4(x,t)}, \tag{25}$$

$$\varrho(t) = \sum_{i=1}^{m}\frac{\varrho_i(t)}{n_i}, \tag{26}$$

$$p(0,t) = \varrho(t), \tag{27}$$

$$\bar{u}_{p,i}\frac{\partial c_i}{\partial x} = -\lambda_f\frac{c_i}{a_i}, \quad \lambda_f = \left(\frac{8D}{\pi\mathcal{R}_0}\right)^{1/4}\frac{\pi D\Lambda}{Q_{\text{pore}}}, \tag{28}$$

$$\frac{\partial a_i}{\partial t} = -c_i, \tag{29}$$

for $1 \le i \le m$, with boundary and initial conditions

$$c_1(0,t) = 1, \quad a_i(x,0) = a_{i_0}, \quad x_{i-1} \le x \le x_i. \tag{30}$$

B. Flow: Constant Pressure Case

In this case, we again nondimensionalize the model (1)–(14), using the same scalings as in (23), except for

$$\begin{aligned} U &= \frac{P_0}{4W^2\mu\mathcal{R}_0}u, \\ \bar{U}_{p,i} &= \left(\frac{P_0^2}{8\pi\mu^2 D\mathcal{R}_0}\right)^{1/2}\bar{u}_{p,i}, \\ V &= \left(\frac{8D}{\pi\mathcal{R}_0^5}\right)^{1/4}\frac{P_0}{\mu\Lambda\alpha C_0}v \end{aligned} \tag{31}$$

Under these scalings, the governing equations for $v(t)$, $\bar{u}_{p,i}(x,t)$, $\varrho(t)$, $u(t)$, $c_i(x,t)$, and $a_i(x,t)$ (i.e., throughput, averaged pore velocity, branching structure resistance, Darcy velocity, averaged particle concentration and pore radius in the ith layer, respectively) become

$$\frac{dv}{dt} = u(t) = n_i a_i^2(x,t)\bar{u}_{p,i}(x,t), \tag{32}$$

$$\varrho_i(t) = \int_{x_{i-1}}^{x_i}\frac{dx}{a_i^4(x,t)}, \tag{33}$$

$$\varrho(t) = \sum_{i=1}^{m}\frac{\varrho_i(t)}{n_i}, \tag{34}$$

$$u(t) = \frac{p(0,t)}{\varrho(t)}, \tag{35}$$

$$\bar{u}_{p,i}\frac{\partial c_i}{\partial x} = -\lambda_p\frac{c_i}{a_i}, \quad \lambda_p = \frac{\Lambda\mu}{P_0}\left(8\pi^3 D^5\mathcal{R}_0^3\right)^{1/4}, \tag{36}$$

$$\frac{\partial a_i}{\partial t} = -c_i, \tag{37}$$

for $1 \le i \le m$, with boundary and initial conditions

$$\begin{aligned} &c_1(0,t) = 1, && a_i(x,0) = a_{i_0}, \quad x_{i-1} \le x \le x_i, \\ &p(0,t) = p_{\text{switch}}, && p(1,t) = 0, \end{aligned} \tag{38}$$

where p_{switch} is the dimensionless prescribed pressure at the pore inlet.

C. Elasticity: Constant Flux Case

We introduce the scalings

$$\begin{aligned} R &= Wr = \varepsilon Dr, \\ (\Omega_{i_R}, \Omega_{i_X}) &= W(\omega_{i_r}, \omega_{i_x}), \\ (P_i, \Sigma_{i_R}, \Sigma_{i_\theta}, \Sigma_{i_X}) &= \mu\mathcal{R}_0 Q_{\text{pore}}(p_i, \sigma_{i_r}, \sigma_{i_\theta}, \sigma_{i_x}), \end{aligned} \tag{39}$$

for $1 \le i \le m$, where $\varepsilon := W/D \ll 1$ is the small aspect ratio of the pores. Note that, we use the same scaling of pressure P_i as in section §III A (see (23)) and scale the normal stresses $\mathbf{\Sigma}_i$ the same way as the pressure P_i. Again, recall that we assumed axisymmetry, so $\Omega_{i_\theta} = 0$ and $\partial(\cdot)/\partial\theta = 0$. Now, the dimensionless versions of equations (17) and (18), via the scalings (23) and (39), are:

$$\begin{aligned} \frac{1}{\varepsilon D}\Bigg\{&\frac{1}{r}\frac{\partial}{\partial r}\left(r\frac{\partial\omega_{i_r}}{\partial r}\right) + \varepsilon^2\frac{\partial^2\omega_{i_r}}{\partial x^2} - \frac{\omega_{i_r}}{r^2} \\ &+ \frac{1}{1-2\nu}\frac{\partial}{\partial r}\left[\frac{1}{r}\frac{\partial\left(r\omega_{i_r}\right)}{\partial r} + \varepsilon\frac{\partial\omega_{i_x}}{\partial x}\right]\Bigg\} = 0, \end{aligned} \tag{40}$$

$$\begin{aligned} \frac{1}{\varepsilon D}\Bigg\{&\frac{1}{r}\frac{\partial}{\partial r}\left(r\frac{\partial\omega_{i_x}}{\partial r}\right) + \varepsilon^2\frac{\partial^2\omega_{i_x}}{\partial x^2} \\ &+ \varepsilon\frac{1}{1-2\nu}\frac{\partial}{\partial x}\left[\frac{1}{r}\frac{\partial}{\partial r}(r\omega_{i_r}) + \varepsilon\frac{\partial\omega_{i_x}}{\partial x}\right]\Bigg\} = 0, \end{aligned} \tag{41}$$

for $1 \le i \le m$. The boundary conditions (19) become

$$\begin{aligned} \sigma_{i_r}|_{r=a_i} &= p_i, & \left.\frac{\partial\sigma_{i_r}}{\partial r}\right|_{r=1} &= 0, \\ \omega_{i_x}|_{x=d_{i-1}} &= 0, & \omega_{i_x}|_{x=d_{i-1}} &= 0, \end{aligned} \tag{42}$$

for $1 \le i \le m$. Equation (20) leads to the dimensionless expression for the r-component of the normal stress:

$$\sigma_{i_r} = \frac{1}{\eta_f}\left[(1-\nu)\frac{\partial\omega_{i_r}}{\partial r} + \nu\frac{\omega_{i_r}}{r} + \varepsilon\nu\frac{\partial\omega_{i_x}}{\partial x}\right], \tag{43}$$

where we have defined

$$\eta_f = \frac{\mu\mathcal{R}_0 Q_{\text{pore}}(1+\nu)(1-2\nu)}{E}, \tag{44}$$

which can be considered as a fluid–structure interaction (or, compliance) parameter[34].

Next, we introduce a perturbation expansion of the dependent variables ω_{i_r}, ω_{i_x}, σ_{i_r} and p_i, in powers of the slenderness parameter $\varepsilon \ll 1$:

$$\begin{aligned} \omega_{i_r}(r,x,t) &= \omega_{i_r}^{(0)}(r,x,t) + \varepsilon\omega_{i_r}^{(1)}(r,x,t) + \cdots, \\ \omega_{i_x}(x,r,t) &= \omega_{i_x}^{(0)}(r,x,t) + \varepsilon\omega_{i_x}^{(1)}(r,x,t) + \cdots, \\ \sigma_{i_r}(r,x,t) &= \sigma_{i_r}^{(0)}(r,x,t) + \varepsilon\sigma_{i_r}^{(1)}(r,x,t) + \cdots, \\ p_i(x,t) &= p_i^{(0)}(x,t) + \varepsilon p_i^{(1)}(x,t) + \cdots. \end{aligned} \tag{45}$$

Substituting these expansions into (40) and (41), at the leading order we have

$$\frac{1}{r}\frac{\partial}{\partial r}\left(r\frac{\partial\omega_{i_r}^{(0)}}{\partial r}\right) - \frac{\omega_{i_r}^{(0)}}{r^2} + \frac{1}{1-2\nu}\frac{\partial}{\partial r}\left(\frac{1}{r}\frac{\partial(r\omega_{i_r}^{(0)})}{\partial r}\right) = 0, \tag{46}$$

$$\frac{1}{r}\frac{\partial}{\partial r}\left(r\frac{\partial\omega_{i_x}^{(0)}}{\partial r}\right) = 0. \tag{47}$$

It is easy to verify that the solution to the last two equations is of the form:

$$\omega_{i_r}^{(0)} = f_1(x)r + \frac{f_2(x)}{r}, \qquad \omega_{i_x}^{(0)} = \frac{f_3(x)}{r}, \tag{48}$$

where $f_1(x)$, $f_2(x)$ and $f_3(x)$ are arbitrary functions of integration to be determined. The leading-order term of equation (43) is

$$\sigma_{i_r}^{(0)} = \frac{1}{\eta_f}\left[(1-\nu)\frac{\partial \omega_{i_r}^{(0)}}{\partial r} + \nu\frac{\omega_{i_r}^{(0)}}{r}\right]. \tag{49}$$

Considering the boundary conditions (42) at leading order, along with (49), we obtain $f_1(x)$, $f_2(x)$ and $f_3(x)$. Therefore, the solution (48) to the differential equations for the radial and axial displacements, at the leading order in ε, simplifies to

$$\omega_{i_r}^{(0)}(r,x,t) = \eta_f\, p_i^{(0)}(x,t)\, r, \qquad \omega_{i_x}^{(0)}(r,x,t) = 0, \tag{50}$$

valid for $a_i \le r \le 1$. Consequently, for the elastic membrane, equation (29) describing the evolution of the pore radius should be updated as

$$\frac{\partial a_i}{\partial t} = -c_i + \eta_f \frac{\partial p_i}{\partial t} r\bigg|_{r=a_i}, \quad a_i(x,0) = a_{i_0}, \tag{51}$$

for $1 \le i \le m$ and $x_{i-1} \le x \le x_i$.

Observe, from (50), that the asymptotic analysis and the clamped boundary conditions on ω_{i_x} lead to $\omega_{i_x}^{(0)}(r,x,t) = 0$ identically at the leading order. This result generically holds for many types of fluid–structure interactions in slender (small aspect ratio) flow conduits. On the other hand, some works on fluid–structure interactions assume no axial displacement in long pores straightaway, which the asymptotic analysis above justifies. Actually, it turns out that axial-clamping and no-axial-displacement are equivalent assumptions for long, slender cylindrical pores, under the lubrication approximation, under which the shear stress on the wall is negligible compared to the pressure (normal stress). Anand and Christov [34] elaborate on this points in detail, in the context of viscous flow in a slender cylindrical shell.

D. Elasticity: Constant Pressure Case

For the case of constant pressure filtration, we use the same scalings as in (23) and (39), but the pressure P_i and the stresses $\mathbf{\Sigma}_i$ are scaled with P_0:

$$(P_i, \mathbf{\Sigma}_i) = P_0(p_i, \sigma_{i_r}, \sigma_{i_\theta}, \sigma_{i_x}). \tag{52}$$

Note that all equation from §III C are valid for the constant pressure scenario, except η_f is replaced by η_p, so that (51) becomes

$$\frac{\partial a_i}{\partial t} = -c_i + \eta_p \frac{\partial p_i}{\partial t} r\bigg|_{r=a_i}, \quad a_i(x,0) = a_{i_0}, \tag{53}$$

for $1 \le i \le m$ and $x_{i-1} \le x \le x_i$, having defined the suitable fluid–structure interaction parameter for this case to be

$$\eta_p = \frac{P_0(1+\nu)(1-2\nu)}{E}. \tag{54}$$

IV. RESULTS

In this section, we present and analyze simulations of the models (24)–(30), (32)–(38), (51) and (53). Our numerical scheme is straightforward, based on first-order accurate finite-difference spatial discretization of the governing equations with implicit time-stepping of the pore-blocking evolution (i.e., (51) and (53)), and trapezoidal quadrature to evaluate the necessary integrals. In our simulation, we consider a process in which, at first, the flux through the membrane is kept constant. In order to sustain the flux, the pressure increases in time. To mimic practical applications, we set a threshold pressure p_{switch}, at which the model transitions to a scenario in which the imposed inlet pressure remains at p_{switch} until the pores close. Thus our simulation is composed of two temporal periods. During the constant flux period, equations (24)–(30) and (51) are solved. Then, upon transitioning to the constant pressure regime, equations (32)–(38) and (53) govern the filtration process. Through simulation, we will demonstrate how the pore radius at each layer $a_i(x,t)$, throughput $v(t)$, flux $q(t)$, and the imposed pressure at the top of the membrane $p(0,t)$ evolve during a typical filtration process. Then, we will present findings on how the filtration performance changes for different values of the compliance coefficients η_f and η_p (defined in (44) and (54)).

To fully specify our model, various dimensional and dimensionless parameters given in Tables I and II, respectively, are estimated based on the typical ranges arising in filtration applications. Specifically, the dimensionless parameters λ_f and λ_p capture the physics of the attraction between particles and the pore walls in the constant flux and constant pressure drop cases, respectively. The

Parameter	Description	Typical value
$2W$	Width of repeating lattice	4.5 μm
μ	Viscosity of feed	0.001 Pa s
Λ	Particle–wall attraction coeff.	Varies
D	Membrane thickness	300 μm
$\mathcal{R}_0$	Initial resistance	10^{13}-10^{15} m^{-3}
Q_{pore}	Flux	2-3 L/h
P_{switch}	Pressure drop	10-100 kPa
C_0	Inlet particle concentration	1-10 g/L
α	Pore shrinkage parameter	Varies
E	Young's modulus	0.1-10 MPa

TABLE I. Dimensional parameter values[5,26,46,47] for the model.

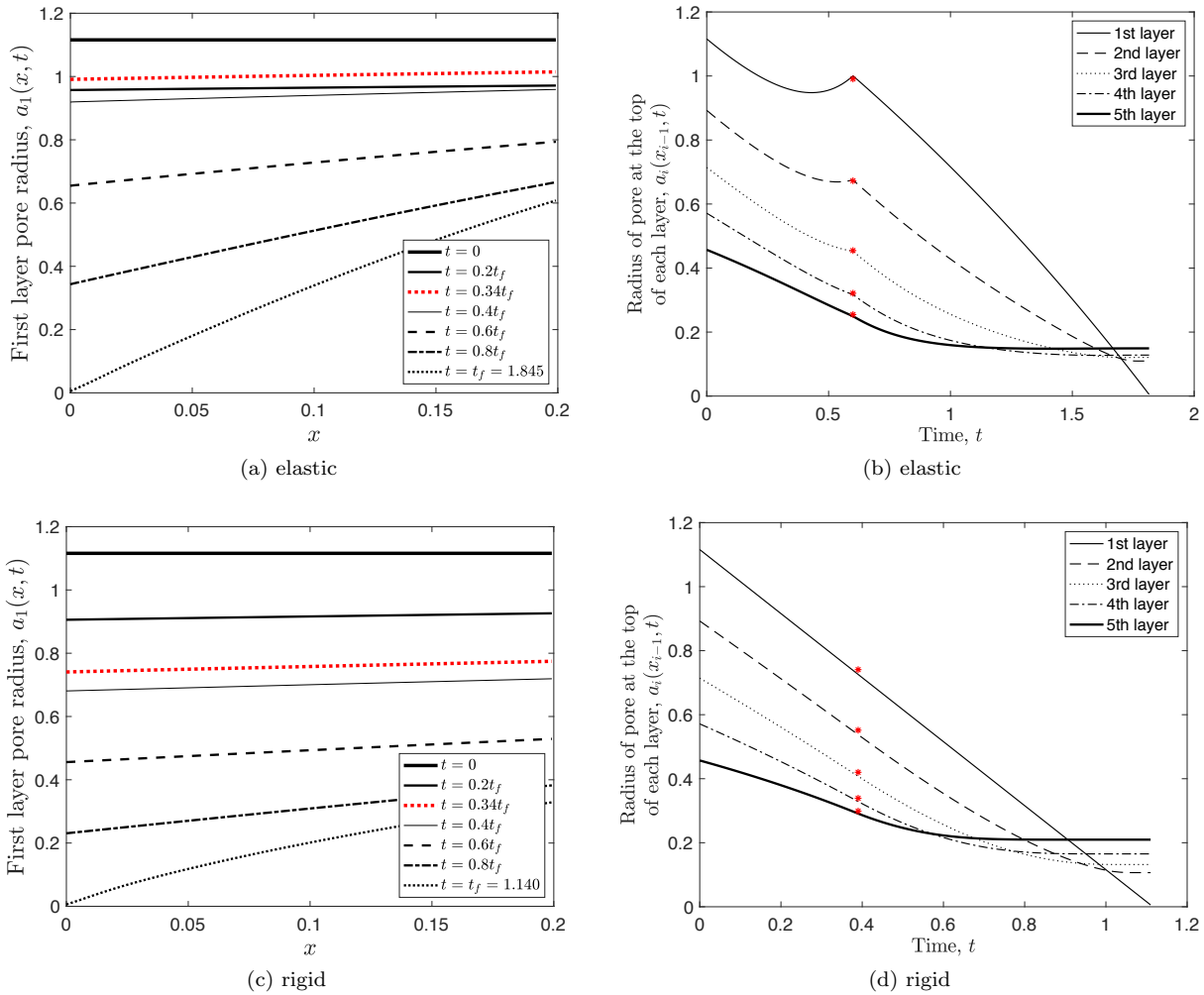

(a) elastic (b) elastic

(c) rigid (d) rigid

FIG. 3. Pore radius variation $a_1(x,t)$ with distance down the filter x in the first layer $i = 1$, at certain times t (the red curves are for the switching time) up to the final blocking time t_f, for a membrane with (a) elastic and (c) rigid pores. Pore radii at the top of each layer $a_i(x_{i-1},t)$ versus time t, for a membrane with (b) elastic and (d) rigid pores. The asterisk in each plot denotes the instant of time at which the filtration process switches from the constant flux to the constant pressure drop regime. In all cases, $\lambda_f = 0.5$, $\lambda_p = 0.5$, $p_{\text{switch}} = 5$, $\varrho_0 = 1$, and the initial pore radius of each layer is geometrically decreasing with coefficient $\kappa = 0.8$. In (a) and (b), we use $\eta_f = 0.005$ and $\eta_p = 0.001$.

Parameter	Formula	Typical value
ε	W/D	10^{-2}
λ_f	$(8D/(\pi\mathcal{R}_0))^{1/4}\ (\pi D\Lambda/Q_{\text{pore}})$	0.5
λ_p	$(\Lambda\mu/P_0)\ (8\pi^3 D^5\mathcal{R}_0^3)^{1/4}$	0.5
ν	Poisson's ratio	0.2-0.3
η_f	$\mu\mathcal{R}_0 Q_{\text{pore}}(1+\nu)(1-2\nu)/E$	0.001-0.01
η_p	$P_0(1+\nu)(1-2\nu)/E$	0.0002-0.002

TABLE II. Dimensionless parameters values[5,26,46,47] for the model.

values vary for different filters and largely depends on the structure and material of the filter membrane. Per prior literature[6,17,26], we take $\lambda_f = 0.5$, $\lambda_p = 0.5$ and $p_{\text{switch}} = 5$ for our simulations. The initial branching resistance is fixed at $\varrho_0 = 1$ and the initial pore radii are geometrically decreasing with coefficient $\kappa = 0.8$, i.e. $a_i(x,0) = a_0\kappa^{i-1}$ for $i \in \{1,2,3,4,5\}$, where a_0 can be obtained by (25) and (26) (or (33) and (34)). Additionally, the dimensionless parameters η_f and η_p describes the compliance of the pores (radius expansion caused by interior pressure) due to their elasticity for constant flux and pressure regimes, respectively. Note that $\lambda_f = \lambda_p$, and $\eta_f = \eta_p\ p_{\text{switch}}$.

Figures 3(a) and (c) show the change of the pore radius in the first layer $a_1(x,t)$ for an elastic and a rigid membrane, respectively, at certain times up to the final blocking time t_f. The red curves in both figures show the pore radius at the time when the filtration process switches from the constant flux driven flow to the

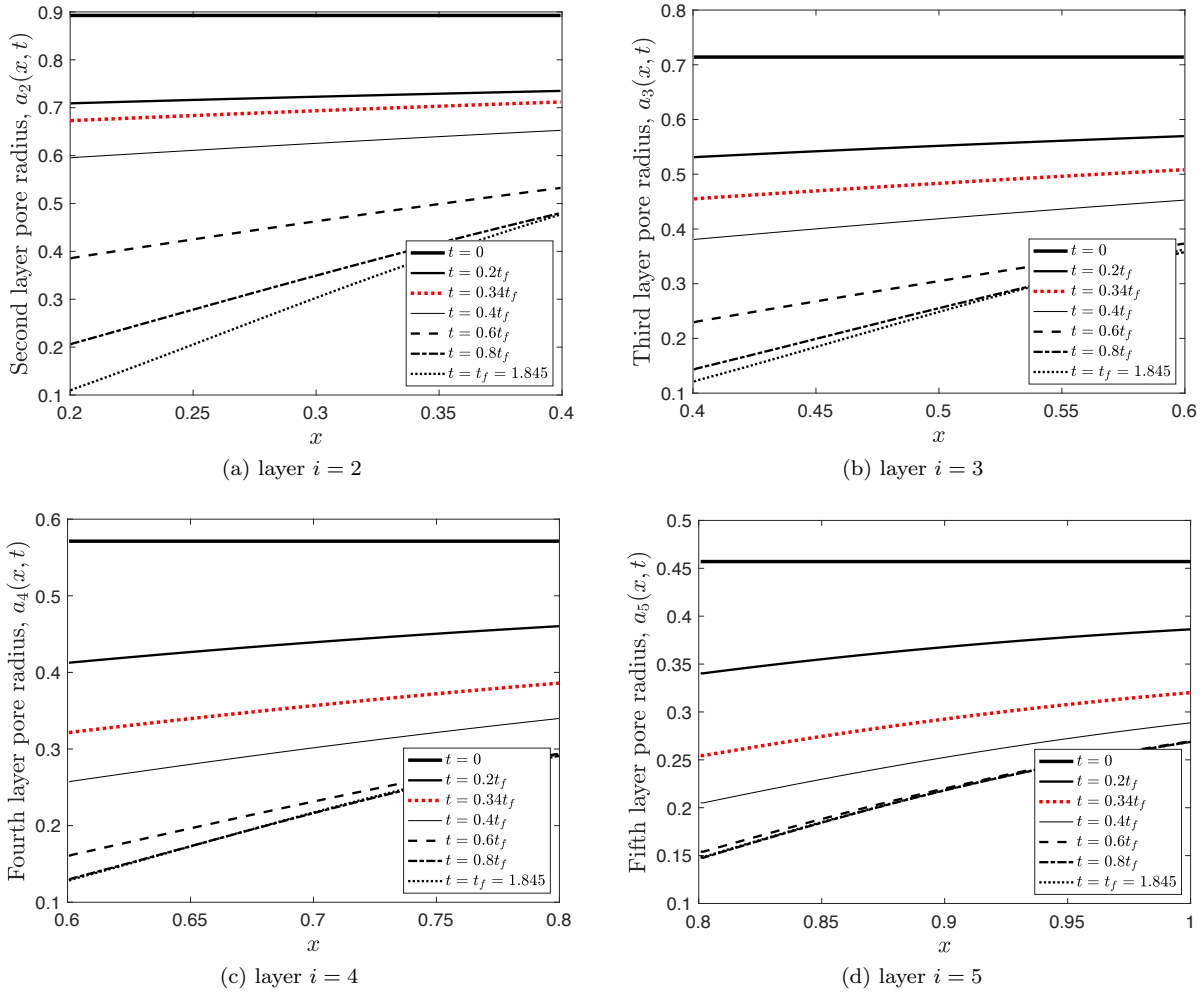

(a) layer $i = 2$ (b) layer $i = 3$

(c) layer $i = 4$ (d) layer $i = 5$

FIG. 4. (a)–(d) Depth-variation of elastic membrane pore radii $a_i(x,t)$ for $i \in \{2,3,4,5\}$ (layers 2-5), respectively, at specific instants of time up to the final blocking time t_f. All panels simulated with $\lambda_f = 0.5$, $\lambda_p = 0.5$, $p_{\text{switch}} = 5$, $\varrho_0 = 1$, $\kappa = 0.8$, $\eta_f = 0.005$, and $\eta_p = 0.001$. The red curves show the pores' radii at the switching time $t = 0.34t_f$.

constant pressure regime. From Fig. 3(a), we conclude that, the pore shrinks relatively uniformly across x during early stages of filtration. Then, as more particles are deposited at the inlet of the pore, the distribution of pore radius over x, gradually becomes steeper, until $a_1(0,t_f) = 0$ at the instant when the pore is completely blocked. We observe that the pore radius has a tendency to expand when the pressure increases, since the pore profiles at $t = 0.2t_f$ and $t = 0.4t_f$ are very close to each other and in both case the pore radii are less than the corresponding ones at the switching time $t = 0.34t_f$, as shown in Fig. 3(a). This observation indicates a conspicuous expansion of the pore radius at the switching time. This phenomenon is explained by the fact that the pore radius evolution is mainly driven by pressure at that point in the filtration process, rather than particle deposition. Generally speaking, the pore radius shrinks at a steady rate in the absence of elasticity, as shown in Fig. 3(c). Note that, due to pore expansion in elastic membranes, the final time of filtration $t_f = 1.845$ for the elastic case, which is larger than $t_f = 1.140$ for the rigid case, as shown in Fig. 3(a) and (c), respectively.

Figures 3(b) and (d) show the evolution of the pore radius at the upstream side of each layer $a_i(x_{i-1},t)$, where $i \in \{1,2,3,4,5\}$, for an elastic and a rigid membrane, respectively. Note that the red asterisks in these figures show the switching point from the constant flux regime to the constant pressure regime. In Fig. 3(d), the pore radius at the top of the first layer shrinks to zero steadily, while the downstream pores shrink more slowly and less uniformly in time. This pattern is consistent with results obtained by Gu *et al.*[4], Sanaei and Cummings[17]. Therefore, we can use the same rationale to explain this phenomenon: when top layers shrink, spatial gradients in the particle concentration increase, leading to a decrease of the closure rate in downstream layers. When we study the two regimes separately, we observe some apparent differences in the radius at the top of the downstream

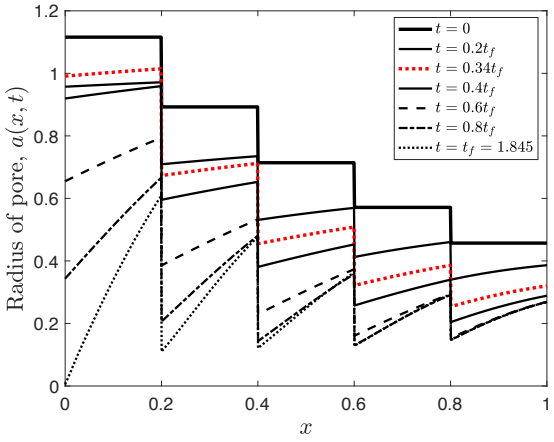

FIG. 5. Elastic membrane pore radius versus depth x at several different instants of time, showing the radii across all layers. Here, $\lambda_f = 0.5$, $\lambda_p = 0.5$, $p_{\text{switch}} = 5$, $\varrho_0 = 1$, $\kappa = 0.8$, $\eta_f = 0.005$, and $\eta_p = 0.001$.

layers, which is more pronounced in the 5th layer. After changing to the constant pressure scenario, the top of the pore in the 5th layer first shrinks with a slower rate (compared to the other layers) and then tends to a constant radius. This phenomenon gradually diminishes as we move up in the layers, to the point that it is not observed in the first layer. This observation is related to the small particle concentration in the feed solution, which will be explained in detail later. When the elasticity of the pores is accounted for, as shown in Fig. 3(b), pore radius expansion is observed. For example, in the first layer, there is an upward tendency compared with the same curve in Fig. 3(d). This stems from the fact that, in the late stage of constant flux scenario, the effect of expansion brought by large pressure compensates for the shrinkage due to deposition of small particles. This phenomenon is less discernible in downstream layers, since pressure decreases along the depth of the branching structure.

To further investigate the novel aspects of the elastic membrane pore shrinkage, we plot representative depth-variation of the pore radii $a_i(x,t)$ ($i \in \{2,3,4,5\}$), for layers 2-5, at some specific instants of time in Fig. 4(a)–(d). These plots collectively show that the pore shrinkage is more pronounced at the upstream end of each layer, which is consistent with the observations from Fig. 3(a). In addition, we notice that the fourth and fifth layers' pore radii do not change close to the final filtration times, for example at $t = 0.8t_f$ and t_f. In all panels of Fig. 4, the pores' radii at the switching time $t = 0.34t_f$ do not expand as much as the first layer's pore radius (at the same instant of time), which was shown before in Fig. 3(a).

To gain more insight into the evolution of the elastic membrane pore radii across all layers, we plot them for several different instants of time in Fig. 5. The initial stage pattern at $t = 0$ represents the whole membrane branching structure. Only one pore in each layer is selected for the figure since all pores in the same layer are identical. Figure 5 more clearly shows the different shrinkage patterns in different layers, and it demonstrates how the membrane's hierarchical bifurcating structure evolves during the filtration process.

Next, in Figs. 6(a) and (b), we show the evolution of the particle concentration at the membrane outlet $c_m(1,t)$, throughout the filtration process in a membrane with and without elasticity, respectively. Again the red asterisks denote the instant of time at which the flow transits from the constant flux scenario to the constant pressure regime. It can be observed that the trend of $c_m(1,t)$ in the constant flux scenario is increasing. Then, after transferring to the constant pressure regime, the small particle concentration drops quickly. This change in trends of $c_m(1,t)$ explains why the pore radius shrinks faster after the filtration process switches to the constant pressure regime. It is evident that the particle concentration remains low for a long time at the final stage of the filtration process, which indicates clogging of the branching structure at that time. Both Figs. 6(a) and (b) show that more particles escape from the elastic membrane, compared to the rigid one, throughout the filtration process, since the closure time t_f is longer for the elastic case.

Note that, during the filtration process, the flux is proportional to the averaged Darcy velocity, therefore the dimensionless flux is given by $q(t) = u(0,t)$. Consequently, the dimensionless throughput is $v(t) = \int_0^t q(t')dt'$, since it is the total filtrate processed and equal to the cumulative flux at time t. Figures 7(a) and (b) show the total flux $q(t)$ and the reciprocal of the pressure drop imposed at the top of the branching model $1/p(0,t)$ versus throughput $v(t)$ for an elastic and a rigid structure, respectively. In both figures, the blue curves (left axes) indicate that at first flux $q(t)$ remains constant until the filtration process changes to the constant pressure regime, then it drops to 0 due to clogging. The orange curves (right axes) represent the inverse of the pressure at the upstream $1/p(0,t)$. It decreases during the constant flux scenario and becomes constant after the process switches to the constant pressure regime.

Figures 7(a) and (b) tell us that, for the elastic structure, the inverse of the pressure at the upstream $1/p(0,t)$ decreases with a smaller slope compared to the rigid membrane, while the flux falls to 0 with almost the same rate in both cases. Moreover, for the elastic membrane in Fig. 7(a), the flux-throughput curve's shape is concave at first and then becomes convex (although it might be harder to see this in Fig. 7(b)), which is consistent with the shape curvature discussed by Giglia and Straeffer [48] for their experiment. Note that, for the elastic membrane, the pressure reaches the threshold value p_{switch} more slowly than the for the rigid membrane; and the whole filtration process lasts longer as well. Thus, our model quantitatively captures the consequences of pore elasticity in the filter. When the pressure increases, the pore radii will expand due to elasticity, allowing more

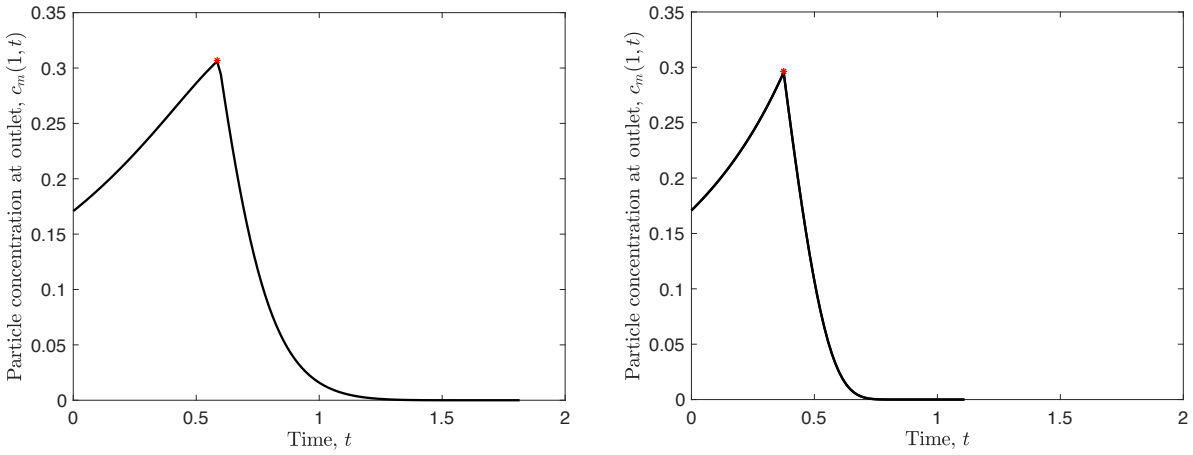

(a) elastic (b) rigid

FIG. 6. Particle concentration at the downstream end, $c(1,t)$, versus time t for a membrane with (a) elastic and (b) rigid pores. Here, $\lambda_f = 0.5$, $\lambda_p = 0.5$, $p_{\text{switch}} = 5$, $\varrho_0 = 1$, $\kappa = 0.8$, $\eta_f = 0.005$, and $\eta_p = 0.001$. The asterisk in each plot denotes the instant of time at which the filtration process switches from the constant flux to the constant pressure drop regime.

fluid to flow through. Then, it takes longer for the elastic pores to shrink and become clogged.

Figure 7(c) shows the throughput $v(t)$ (left axis) and particle concentration at the outlet of each layer $c_i(x_i,t)$ for $i \in \{1,2,3,4,5\}$ (right axis) versus time t. Note that the throughput curve is monotonic but its slope decreases with time due to clogging, meaning that the filter performance ultimately deteriorates, as expected. The curves representing the particle concentration at the outlet of each layer $c_i(x_i,t)$ show that the concentration of particles decreases along the depth of the membrane after switching to the constant pressure scenario. This happens with steeper slopes as we move towards the top layers, resulting in faster pore closure there. Our observations here are consistent with the ones for Fig. 3(d), showing that the top of the pore in the 5th layer first shrinks at a slower rate (compared to the other layers) and then tends to a constant radius.

Figures 8(a) and (b) show the flux $q(t)$ versus time t and throughput $v(t)$, respectively, for several different values of the compliance coefficient η_f. Note that η_f and η_p can not be changed independently, since they are related by $\eta_f = \eta_p\, p_{\text{switch}}$ (recall (44) and 54)). The simulation starts in the constant flux scenario, thus $q(t)$ remains constant until the flow is switched to the constant pressure regime. We observe that as η_f increases, the transition point moves to larger t (and, consequently, we achieve larger $v(t)$). This observation can be explained by, once again appealing to the membrane's elasticity. The constant flux scenario lasts longer because it takes longer to reach the same p_{switch}. In addition, as should be expected, the filtration process lasts longer, and more filtrate is processed for larger values of η_f (and, thus, η_p), as shown in Fig. 9, in which the dependence of t_f and $v(t_f)$ on η_f are quantified.

V. CONCLUSION

In this paper, we derived a mathematical model of a membrane filter with a branching hierarchical structure composed of elastic pores. Using our model, we analyzed the filtration performance of such a filter. In particular, taking adsorption of small particles at pore walls of the membrane as the dominant mechanism of blocking during the filtration process, we addressed the impact of the hierarchical bifurcating interior morphology and the elastic pore wall properties on the filtration performance. Simulations of the filtration model performed involved two stages: (i) filtration under constant flux until the pressure drop reaches a threshold value, then (ii) filtration switches to a constant pressure drop scenario. Through analysis, scaling and simulations, we showed that the key model parameters that determine filtration performance are the dimensionless attraction coefficients λ_f and λ_p (for constant flux and constant pressure drop conditions, respectively) between the pore wall and particles. In addition, the dimensionless fluid–structure interaction parameters η_f and η_p, which describe the elastic wall's compliance under constant flux and constant pressure drop scenarios, respectively, were found to have a strong influence on filtration performance.

In simulations, we first applied the constant flow condition, for which the pressure increases to sustain the flow. Then, we set a threshold pressure p_{switch}, at which the model switches to the scenario in which the constant pressure p_{switch} is maintained until the pores close (the filter clogs). Due to the hierarchical branching morphology, membrane fouling affects the pore sizes in each layer differently. Our model quantitatively captures the evolution of these pore radii. Importantly, for the prototypical membrane filter mechanical properties and flow conditions considered in this work (recall Tables I and II), we

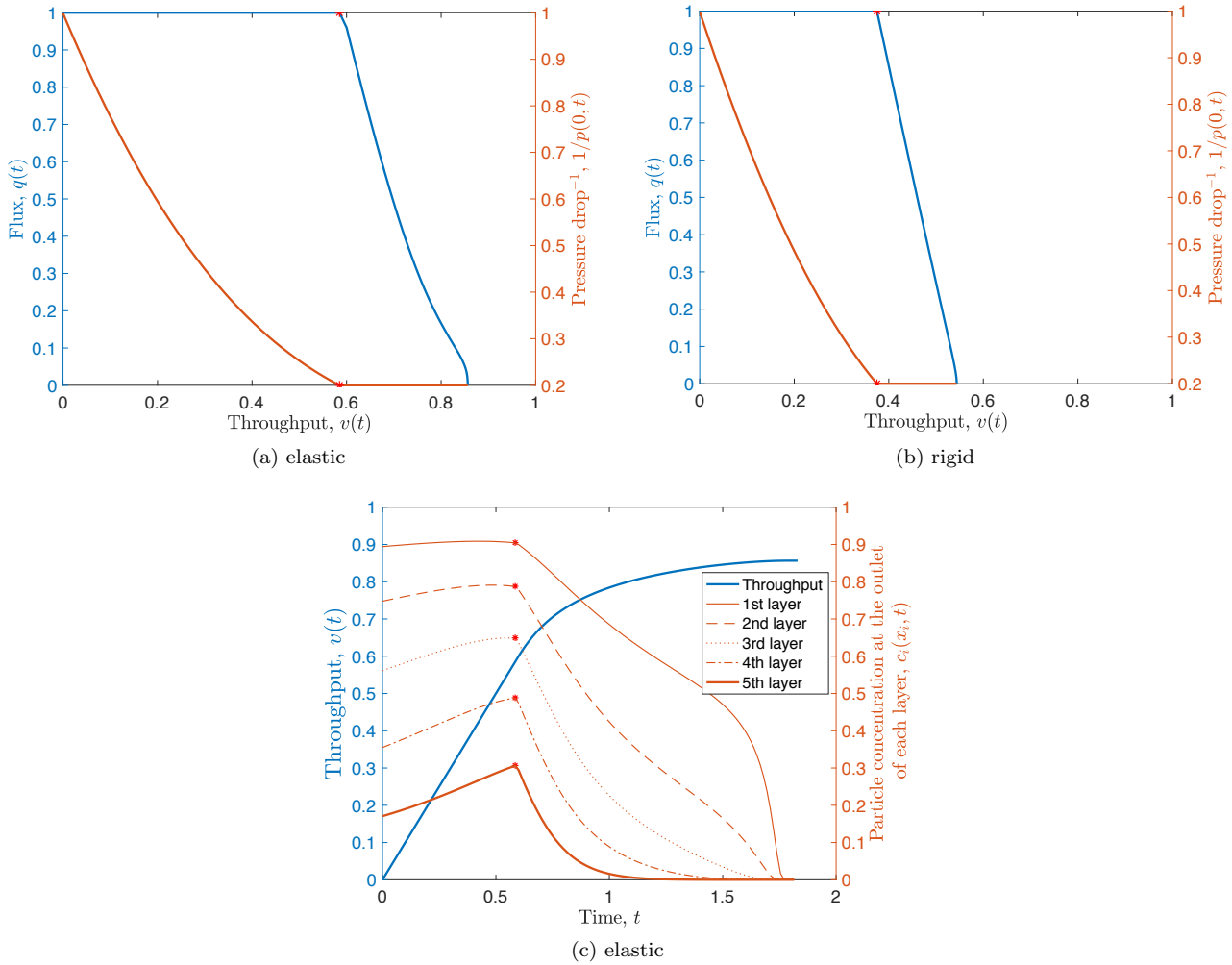

FIG. 7. The flux $q(t)$ (left axis) and the inverse of the pressure drop imposed at the upstream $1/p(0,t)$ (right axis) versus throughput $v(t)$ for a membrane with (a) elastic and (b) rigid pores. (c) Throughput $v(t)$ (left axis) and particle concentration at the outlet of each layer $c_i(x_i,t)$ for $i \in \{1,2,3,4,5\}$ (right axis) versus time t. Here, $\lambda_f = 0.5$, $\lambda_p = 0.5$, $p_{\text{switch}} = 5$, $\varrho_0 = 1$, $\kappa = 0.8$, $\eta_f = 0.005$, $\eta_p = 0.001$.

showed that the balance between pore radius shrinkage by particle absorption and its expansion by pressure (due compliance of the elastic pore walls) delays fouling. Interestingly, as seen by comparing, e.g., Fig. 3(b) and (d), compliance of the pores leads to a transition from decreasing pore radius with time (as the pores clog) back to an *increasing* radius (expansion of the pores) near the switching time from constant flux to constant pressure operation.

Comparing the filtration performance through the particle concentration at the downstream end of the membrane, we showed that the flux drops rapidly to zero for rigid pores, while the flux remains largely unimpeded in the case of elastic pores. In particular, the elastic membrane remains viable (i.e., maintains flow) beyond the time of clogging of the rigid-pore structure. Therefore, we conclude that the elastic pores enable the whole filtration process to last longer. For example, comparing Fig. 8(a) and (b), we see that the total filtration time can be increased significantly. As expected, larger values of η_f and η_p (corresponding to more compliant pores) allow for a longer duration of the filtration process and, consequently, a greater total throughput $q(t)$. In particular, our model predicts a strong (greater than linear) dependence of the filtration time t_f and total throughput $v(t_f)$ on η_f (see Fig. 9, in which an increase by a factor of almost two is achieved in t_f over the range of η_f shown), which has important implications for filter design.

Our model only considered one of the three common fouling mechanisms: adsorption of small particles. Blocking by large particles and cake formation can affect the filtration process as well. Therefore, incorporating these latter two fouling mechanisms is a worthwhile direction for future research. In addition, the branching structure can also be generalized. Our study on only addressed the performance of filtration through a symmetric hier-

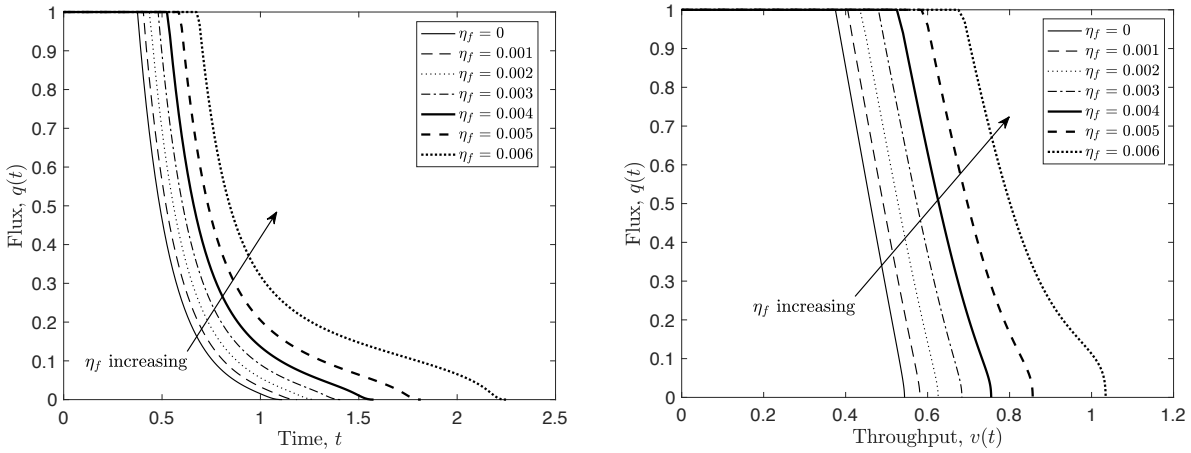

FIG. 8. Flux $q(t)$ versus (a) time t, and versus (b) throughput $v(t)$, for several values of η_f, with $\eta_p = \eta_f\ p_{\text{switch}}$. Here, $\lambda_f = 0.5$, $\lambda_p = 0.5$, $p_{\text{switch}} = 5$, $\varrho_0 = 1$ and $\kappa = 0.8$.

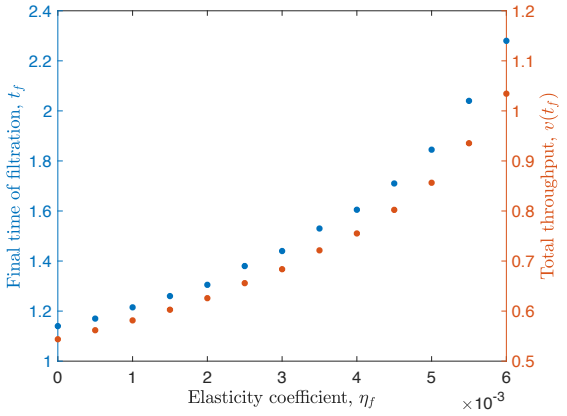

FIG. 9. Total time of filtration t_f (left) and total throughput $v(t_f)$ (right) versus the elastic compliance coefficient η_f for $\lambda_f = 0.5$, $\lambda_p = 0.5$, $p_{\text{switch}} = 5$ and $\varrho_0 = 1$.

archical branching membrane structure. Real membrane filters can have more complex, irregular pore morphology (recall Fig. 1). Therefore, in future work, it would be relevant to study an asymmetric branching model with a, possibly irregular, network of bifurcations and pore connections. It would also be of interest to incorporate our perturbative analytical solution for evolution of elastic pores (recall §III C) into broader pore-network models of multiphase flow in porous media[49], which do not consider pore deformation due to pressure. In this respect, it would also be insightful to incorporate our modeling into a systems engineering framework for industrial design considerations in the future. For example, in some applications, the filter might be replaced or cleaned before switching from the constant flow to the constant pressure drop scenarios. Whether to clean or exchange a filter is based on financial considerations, as well as how practical it is to do so in a given industrial device. On a longer research horizon, a techno-economical analysis of filtration operations, which might determine best practices, could be informed by our fundamental physical modeling.

Acknowledgements

The authors gratefully acknowledge support from the following sources: Z.C. and S.Y.L. from the Summer Undergraduate Research Experience offered by Courant Institute, New York University; I.C.C. from NSF grant CBET-1705637 and the donors of the American Chemical Society Petroleum Research Fund under award # 57371-DNI9; P.S. from the NSF Research Training Group in Modeling and Simulation RTG/DMS-1646339 as well as an Institutional Support of Research and Creativity (ISRC) grant provided by New York Institute of Technology.

Data Availability Statement

Data that support the findings of this study are available within the article. Further information is available from the corresponding author upon reasonable request.

[1] R. W. Baker, *Membrane Technology and Applications*, 2nd ed. (John Wiley & Sons, Chichester, England, 2012).
[2] S. Y. Liu, Z. Chen, and P. Sanaei, "Effects of particles diffusion on membrane filters performance," Fluids **5**, 121 (2020).
[3] E. Iritani, "A review on modeling of pore-blocking behaviors of membranes during pressurized membrane filtration," Drying Technology **31**, 146–162 (2013).
[4] B. Gu, D. L. Renaud, P. Sanaei, L. Kondic, and L. J. Cummings, "On the influence of pore connectivity on performance of membrane filters," Journal of Fluid Mechanics **902**, A5 (2020).

[5]Y. Sun, P. Sanaei, L. Kondic, and L. J. Cummings, "Modeling and design optimization for pleated membrane filters," Physical Review Fluids **5**, 044306 (2020).

[6]P. Sanaei and L. J. Cummings, "Membrane filtration with multiple fouling mechanisms," Physical Review Fluids **4**, 124301 (2019).

[7]D. Fong, L. J. Cummings, S. J. Chapman, and P. Sanaei, "On the performance of multilayered membrane filters," Journal of Engineering Mathematics **127**, 23 (2021).

[8]P. Sanaei, G. Richardson, W. Tom, and L. Cummings, "Flow and fouling in a pleated membrane filter," Journal of Fluid Mechanics **795**, 36–59 (2016).

[9]G. Tchobanoglous, J. Darby, K. Bourgeous, J. McArdle, P. Genest, and M. Tylla, "Ultrafiltration as an advanced tertiary treatment process for municipal wastewater," Desalination **119**, 315–321 (1998).

[10]J. Decarolis, S. Hong, and J. Taylor, "Fouling behavior of a pilot scale inside-out hollow fiber UF membrane during dead-end filtration of tertiary wastewater," Journal of Membrane Science **191**, 165–178 (2001).

[11]J. A. Fernando and D. D. L. Chung, "Pore structure and permeability of an alumina fiber filter membrane for hot gas filtration," Journal of Porous Materials **9**, 211–219 (2002).

[12]B. Veleirinho and J. A. Lopes-da Silva, "Application of electrospun poly (ethylene terephthalate) nanofiber mat to apple juice clarification," Process Biochemistry **44**, 353–356 (2009).

[13]Y. Osada and T. Nakagawa, *Membrane Science and Technology* (CRC Press, 1992).

[14]B. Blankert, B. H. L. Betlem, and B. Roffel, "Dynamic optimization of a dead-end filtration trajectory: Blocking filtration laws," Journal of Membrane Science **285**, 90–95 (2006).

[15]A. Grenier, M. Meireles, P. Aimar, and P. Carvin, "Analysing flux decline in dead-end filtration," Chemical Engineering Research and Design **86**, 1281–1293 (2008).

[16]C.-C. Ho and A. L. Zydney, "A combined pore blockage and cake filtration model for protein fouling during microfiltration," Journal of Colloid and Interface Science **232**, 389–399 (2000).

[17]P. Sanaei and L. J. Cummings, "Membrane filtration with complex branching pore morphology," Physical Review Fluids **3**, 094305 (2018).

[18]H. P. Grace, "Structure and performance of filter media. I. The internal structure of filter media," AIChE Journal **2**, 307–315 (1956).

[19]K. Xiao, Y. Shen, and X. Huang, "An analytical model for membrane fouling evolution associated with gel layer growth during constant pressure stirred dead-end filtration," Journal of Membrane Science **427**, 139–149 (2013).

[20]A. Rahimpour and S. S. Madaeni, "Polyethersulfone (PES)/cellulose acetate phthalate (CAP) blend ultrafiltration membranes: preparation, morphology, performance and antifouling properties," Journal of Membrane Science **305**, 299–312 (2007).

[21]S. P. Deshmukh and K. Li, "Effect of ethanol composition in water coagulation bath on morphology of PVDF hollow fibre membranes," Journal of Membrane Science **150**, 75–85 (1998).

[22]W. J. Bruining, "A general description of flows and pressures in hollow fiber membrane modules," Chemical Engineering Science **44**, 1441–1447 (1989).

[23]I. M. Griffiths, A. Kumar, and P. S. Stewart, "Designing asymmetric multilayered membrane filters with improved performance," Journal of Membrane Science **511**, 108–118 (2016).

[24]I. M. Griffiths, A. Kumar, and P. S. Stewart, "A combined network model for membrane fouling," Journal of Colloid and Interface Science **432**, 10–18 (2014).

[25]M. Dalwadi, M. Bruna, I. M. Griffiths, *et al.*, "A multiscale method to calculate filter blockage," Journal of Fluid Mechanics **809**, 264–289 (2016).

[26]P. Sanaei and L. J. Cummings, "Flow and fouling in membrane filters: effects of membrane morphology," Journal of Fluid Mechanics **818**, 744 (2017).

[27]M. P. Dalwadi, I. M. Griffiths, and M. Bruna, "Understanding how porosity gradients can make a better filter using homogenization theory," Proceedings of the Royal Society A: Mathematical, Physical and Engineering Sciences **471**, 20150464 (2015).

[28]S. Ling, Z. Qin, W. Huang, S. Cao, D. L. Kaplan, and M. J. Buehler, "Design and function of biomimetic multilayer water purification membranes," Science Advances **3**, e1601939 (2017).

[29]Y.-C. Fung, *Biomechanics: Circulation*, 2nd ed. (Springer-Verlag, 1997).

[30]M. E. Rosti, S. Pramanik, L. Brandt, and D. Mitra, "The breakdown of Darcy's law in a soft porous material," Soft Matter **16**, 939–944 (2020).

[31]J. G. Herterich, I. M. Griffiths, and D. Vella, "Reproducing the pressure–time signature of membrane filtration: The interplay between fouling, caking, and elasticity," Journal of Membrane Science **577**, 235–248 (2019).

[32]J. Köry, A. U. Krupp, C. P. Please, and I. M. Griffiths, "The effect of compressibility on the behaviour of filter media," IMA Journal of Applied Mathematics **85**, 564–583 (2020).

[33]J. Köry, A. Krupp, C. Please, and I. Griffiths, "Optimising dead-end cake filtration using poroelasticity theory," Modelling **2**, 18–42 (2021).

[34]V. Anand and I. C. Christov, "Revisiting steady viscous flow of a generalized Newtonian fluid through a slender elastic tube using shell theory," Zeitschrift für Angewandte Mathematik und Mechanik **101**, e201900309 (2021).

[35]V. Anand and I. C. Christov, "On the deformation of a hyperelastic tube due to steady viscous flow within," in *Dynamical Processes in Generalized Continua and Structures*, Springer Series on Advanced Structured Materials, Vol. 103, edited by H. Altenbach, A. Belyaev, V. A. Eremeyev, A. Krivtsov, and A. V. Porubov (Springer Nature, Cham, Switzerland, 2019) Chap. 2, pp. 17–35.

[36]V. Anand and I. C. Christov, "Transient compressible flow in a compliant viscoelastic tube," Phys. Fluids **32**, 112014 (2020).

[37]K. Raj M, J. Chakraborty, S. DasGupta, and S. Chakraborty, "Flow-induced deformation in a microchannel with a non-Newtonian fluid," Biomicrofluidics **12**, 034116 (2018).

[38]P. Karan, S. S. Das, R. Mukherjee, J. Chakraborty, and S. Chakraborty, "Flow and deformation characteristics of a flexible microfluidic channel with axial gradients in wall elasticity," Soft Matter **16**, 5777–5786 (2020).

[39]E. Boyko, M. Bercovici, and A. D. Gat, "Viscous-elastic dynamics of power-law fluids within an elastic cylinder," Physical Review Fluids **2**, 073301 (2017).

[40]A. Dana, Z. Zheng, G. G. Peng, H. A. Stone, H. E. Huppert, and G. Z. Ramon, "Dynamics of viscous backflow from a model fracture network," Journal of Fluid Mechanics **836**, 828–849 (2018).

[41]A. Dana, G. G. Peng, H. A. Stone, H. E. Huppert, and G. Z. Ramon, "Backflow from a model fracture network: an asymptotic investigation," Journal of Fluid Mechanics **864**, 899–924 (2019).

[42]C.-Y. Lai, Z. Zheng, E. Dressaire, G. Z. Ramon, H. E. Huppert, and H. A. Stone, "Elastic relaxation of fluid-driven cracks and the resulting backflow," Physical Review Letters **117**, 268001 (2016).

[43]K.-J. Hwang and T.-T. Lin, "Effect of morphology of polymeric membrane on the performance of cross-flow microfiltration," Journal of Membrane Science **199**, 41–52 (2002).

[44]C. Truesdell and W. Noll, *The Non-Linear Field Theories of Mechanics*, 2nd ed. (Springer-Verlag, 1992).

[45]P. Howell, G. Kozyreff, and J. Ockendon, *Applied Solid Mechanics* (Cambridge University Press, Cambridge, UK, 2009).

[46]J. Cappello, V. d'Herbemont, A. Lindner, and O. Du Roure, "Microfluidic in-situ measurement of Poisson's ratio of hydrogels," Micromachines **11**, 318 (2020).

[47]M. Miyoshi, S. Morisada, K. Ohto, and H. Kawakita, "Recovery of filtered particles by elastic flat-sheet membrane with cross flow," Membranes **11**, 71 (2021).

[48]S. Giglia and G. Straeffer, "Combined mechanism fouling model and method for optimization of series microfiltration performance," Journal of Membrane Science **417**, 144–153 (2012).

[49] J. Gostick, M. Aghighi, J. Hinebaugh, T. Tranter, M. A. Hoeh, H. Day, B. Spellacy, M. H. Sharqawy, A. Bazylak, A. Burns, W. Lehnert, and A. Putz, "OpenPNM: A pore network modeling package," Computing in Science & Engineering **18**, 60–74 (2016).